

Photodisintegration of ${}^6\text{Li}$

W. A. Wurtz

Department of Physics and Engineering Physics, University of Saskatchewan, Saskatoon, Saskatchewan S7N 5E2, Canada and Canadian Light Source, 44 Innovation Boulevard, Saskatoon, Saskatchewan S7N 2V3, Canada

R. E. Pywell*

Department of Physics and Engineering Physics, University of Saskatchewan, Saskatoon, Saskatchewan S7N 5E2, Canada

B. E. Norum and S. Kucuker

Department of Physics, University of Virginia, Charlottesville, Virginia 22904-4714, USA

B. D. Sawatzky

*Temple University/Jefferson Laboratory Newport News, Virginia 23606, USA*H. R. Weller and S. Stave[†]*Triangle Universities Nuclear Laboratory, Duke University, Durham, North Carolina 27708-0308, USA*

M. W. Ahmed

Triangle Universities Nuclear Laboratory, Duke University, Durham, North Carolina 27708-0308, USA and Department of Physics, North Carolina Central University, Durham, North Carolina 27707, USA

(Received 23 May 2013; revised manuscript received 4 June 2014; published 25 July 2014)

The cross sections for the photodisintegration of ${}^6\text{Li}$ have been measured for all the available reaction channels that have neutrons in the final state, except the ${}^6\text{Li}(\gamma, p_0){}^5\text{He}(\text{g.s.})$ channel. The cross sections were measured at the photon energies, 8, 9, 10, 11, 12, 13, 15, and 15.6 MeV using linearly polarized photons, and 20, 25, 30, and 35 MeV using circularly polarized photons. Associated Legendre function coefficients are extracted for the ${}^6\text{Li}(\gamma, n_0){}^5\text{Li}(\text{g.s.})$ and ${}^6\text{Li}(\gamma, n_1){}^5\text{Li}(1.49)$ channels. For all observed reaction channels Legendre function parametrizations are used to determine total cross sections. Comparisons with recent theoretical calculations of the total photodisintegration cross section using various nucleon-nucleon interactions are inconclusive because of the large uncertainty in the cross sections for reactions channels that are not measured. We hope that the precision of our results for specific reaction channels will prompt calculations for those reaction channels.

DOI: [10.1103/PhysRevC.90.014613](https://doi.org/10.1103/PhysRevC.90.014613)

PACS number(s): 25.20.Dc, 24.70.+s, 25.10.+s, 27.20.+n

I. INTRODUCTION

We have experimentally studied the photoneutron reaction channels for ${}^6\text{Li}$. The purpose of this measurement is to supply data for comparison to theoretical calculations. For instance, the Lorentz integral transform method [1] has been applied to the total photodisintegration cross sections of the $A \leq 7$ nuclei [2] and to the individual photoneutron and photoproton reaction channels of ${}^4\text{He}$ [3]. Such calculations have used various formulations of the nucleon-nucleon interaction. Sufficiently precise experimental results can differentiate between nucleon-nucleon interaction formulations and therefore shed light on the underlying nuclear dynamics. However, a lack of experimental data makes comparisons to calculations for specific reaction channels impossible for nuclei with $A > 4$. Calculations have been performed for ${}^6\text{Li}$ by Bacca *et al.* [4] but only for the total photoabsorption cross section.

Our aim is to provide high quality cross section data for specific photodisintegration reaction channels for ${}^6\text{Li}$ to prompt theoretical calculations of those reaction channels.

II. EXPERIMENTAL APPARATUS AND METHODS

The experimental method is similar to that reported in a recent measurement of the ${}^7\text{Li}(\gamma, n_0){}^6\text{Li}(\text{g.s.})$ cross section [5]. However the existence of many competing photoneutron reaction channels for ${}^6\text{Li}$, which cannot be isolated experimentally, necessitates a different approach to the data analysis that will be described here.

A. The High Intensity Gamma-Ray Source

The High Intensity Gamma-Ray Source (HIGS) [6], located on the Duke University campus in Durham, North Carolina, USA, is a facility with the capability of producing essentially monochromatic, polarized γ -ray photons. It uses an electron storage ring and produces ultraviolet photons using a free electron laser (FEL). These ultraviolet photons are then reflected by the downstream FEL mirror toward a second electron bunch in the storage ring. The ultraviolet photons Compton backscatter

*rob.pywell@usask.ca

[†]Present address: Pacific Northwest National Laboratory, P.O. Box 999, Richland, WA 99352, USA.

from the stored electrons, and are promoted to γ -ray energies. The gamma rays arrive in bunches at a frequency of 5.58 MHz or about 180 ns apart, which is determined by the accelerator configuration.

The energy distribution of a produced γ -ray photon is

$$E_\gamma \simeq \frac{4\gamma^2 E_{uv}}{1 + (\gamma\theta)^2 + 4\gamma \frac{E_{uv}}{m_e c^2}}, \quad (1)$$

where E_γ is the energy of the resulting γ -ray photon, E_{uv} is the energy of the incident ultraviolet photon, m_e is the mass of the electron, $\gamma = E_e/m_e c^2$, where E_e is the electron's energy and θ is the angle between the electron's momentum vector and the momentum vector of the produced γ -ray photon. Compton backscattering produces γ -ray photons with the same polarization as the initial ultraviolet photons and the energy resolution is approximately given by

$$\Delta E_\gamma / E_\gamma \simeq (\gamma\theta)^2. \quad (2)$$

Since the energy resolution is proportional to θ we can improve the resolution by selecting a smaller γ -ray beam collimator and accepting a reduced flux.

Two insertion devices were available for use in the FEL. The OK-4 is a planar device capable of producing linearly polarized photons while the OK-5 is a helical device that can produce photons of an arbitrary polarization [7,8]. For the measurements performed between 30 June to 3 July 2008 with energies $8 \text{ MeV} \leq E_\gamma \leq 15.6 \text{ MeV}$, the available γ -ray beam used the OK-4 producing linearly polarized photons. For the measurements performed between 1 October to 3 October 2008, with energies $20 \text{ MeV} \leq E_\gamma \leq 35 \text{ MeV}$, the OK-5 producing circularly polarized photons was available.

B. The target

A ${}^6\text{Li}$ target was built by casting enriched (>99%) ${}^6\text{Li}$ inside a hollow teflon tube. The target ends were capped using thin layers of polyvinyl chloride (PVC) and aluminum. The enriched ${}^6\text{Li}$ was salvaged from a target used previously [9].

The design diameter of 4.1 cm was chosen to accommodate a larger photon beam than the one used in this measurement. A 2.5 cm diameter photon beam was chosen to improve energy resolution. A target length of 12.7 cm was chosen based on the amount of ${}^6\text{Li}$ available. The thickness of the target gave a good neutron production rate while causing minimal time-of-flight resolution degradation.

A second target housing was constructed and left empty for use with background subtraction measurements. Using this target we found that the target windows were thin enough that they produced negligible numbers of neutrons. However, we found that the photodisintegration of atmospheric nitrogen produced a significant number of neutrons so that a background subtraction was necessary for photon energies $E_\gamma \geq 20 \text{ MeV}$.

A natural lithium (92% ${}^7\text{Li}$) target was also constructed and measurements using that target were made in the same data-taking period. Results obtained with the ${}^7\text{Li}$ target are reported elsewhere [5,10].

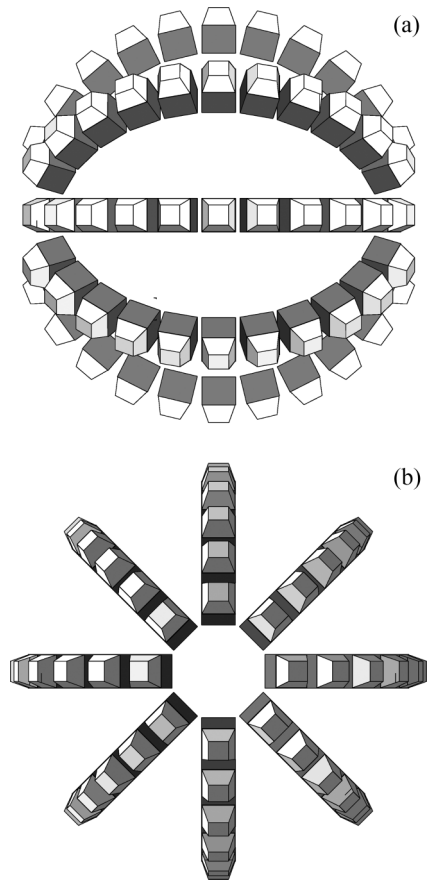


FIG. 1. The arrangement of neutron detectors in the Blowfish Neutron Detector Array. (a) Beam left to right. (b) Beam into page.

C. The Blowfish Neutron Detector Array

The Blowfish Neutron Detector Array [11], or Blowfish for short, is a joint project between the University of Saskatchewan and the University of Virginia. It is housed at the HIGS facility. Blowfish consists of 88 neutron detector cells arranged in a spherical shell with radius 40.6 cm covering a solid angle of about $1/4$ of 4π sr, as shown in Fig. 1.

The detectors use the liquid scintillator BC-505 for which we have previously studied the light output characteristics [12]. BC-505 provides good pulse-shape discrimination (PSD) and can be stored in acrylic containers. Each detector cell has an active volume of $7.6 \times 7.6 \times 6.4 \text{ cm}^3$. They are coupled to photomultiplier tubes via acrylic light guides and silicone wafers.

The gains of the neutron detectors were obtained using gamma rays from radioactive sources. These calibrations were normally done at the beginning and end of each day of data acquisition. A fiber-optic gain monitoring system can be used to continuously monitor the gain of each detector cell photomultiplier tube [13]. The gain monitoring system was unavailable for the measurements with photon energies $8 \text{ MeV} \leq E_\gamma \leq 15.6 \text{ MeV}$ but it was used for the measurements with photon energies $20 \text{ MeV} \leq E_\gamma \leq 35 \text{ MeV}$. When the gain monitoring system was not available, more frequent calibrations using radioactive sources were performed by

periodically stopping the accelerator. An uncertainty in the gain translates into an uncertainty in the light-output threshold used in the analysis, which in turn determines the neutron detection efficiency. Observed changes in gain from the calibration runs allow uncertainties to be estimated which are included in our reported systematic uncertainties.

D. Data acquisition

The photomultiplier signal from each scintillator cell was passed through a constant fraction discriminator (CFD). The analog signal was further split and passed to two separate VME charge-to-digital converters (QDCs), each of which had a different charge integrating gate width to allow pulse shape discrimination (PSD). The logic output from each CFD was passed to the stop of a VME time-to-digital converter (TDC). The start signal to the TDC was derived from an accelerator signal linked to the arrival time of each photon bunch. This allowed the time-of-flight of neutrons from the target to the Blowfish cell to be determined.

The Lucid data acquisition system [14,15] was used. This allowed the simultaneous recording of scaler information for diagnostic purposes and flux normalization, as well as different event types associated with the gain monitoring system.

E. Spectra

We obtained three principle spectra which we used in our data analysis: light-output spectra, time-of-flight spectra and pulse-shape discrimination (PSD) spectra. The light-output spectra were calculated from the gain-calibrated output of our charge-to-digital converters (QDCs). A low-energy threshold was placed on the light-output in the analysis. A threshold that is too low suffers from increased noise and room background while a threshold that is too high misses important low-energy neutrons and decreases the detector efficiency.

We computed time-of-flight from the TDC spectrum obtained using a start signal from an accelerator beam-position monitor and stop signals from individual detectors. The start signal was the arrival time of the photons at the target plus a constant offset. An example TDC spectrum for an individual Blowfish cell is shown in Fig. 2. Time-of-flight was useful for eliminating most of the γ rays from our spectra. We typically performed a hardware time cut to eliminate the large γ -ray peak visible in Fig. 2. These γ rays were primarily due to photons that were Compton scattered from the target. This cut decreases our dead time and increases our sensitivity to neutrons. Further elimination of γ rays can be done using PSD.

We perform PSD by comparing the output of the QDCs used to compute the light-output spectra (the “long gate” QDC) and QDCs which integrate over only part of the PMT pulse (the “short gate” QDC). Since γ rays and neutrons produce pulses with different fall times, we can distinguish between them by computing a PSD parameter related to the difference between the long and short gate QDC values. We computed the PSD parameter such that, nominally, γ rays have a negative PSD parameter and neutrons have a positive PSD parameter. In this way appropriate cuts on the PSD parameter value and the light

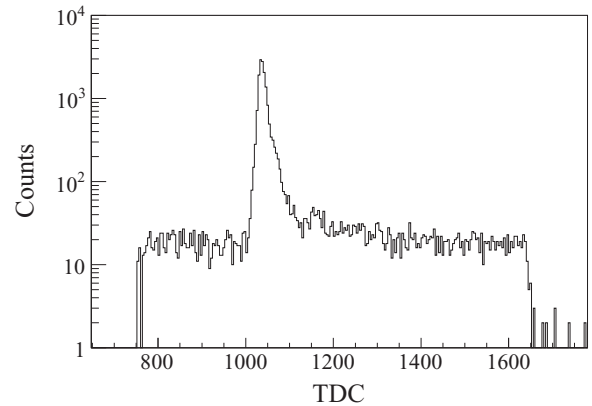


FIG. 2. An example TDC spectrum with a log scale on the vertical axis. One TDC unit on the horizontal axes corresponds to a nominal 0.1 ns. The peak is due to γ rays Compton scattering from the target. There is a small neutron contribution to the right of the peak. The drops to zero on either side are due to hardware windowing.

output can eliminate γ rays from our spectra, but care must be taken as these cuts can also eliminate some neutrons. A sample PSD scatter plot can be found in Fig. 3. Notice that low light-output events cannot be separated using the PSD parameter. We ensure that our light-output cut is high enough that good separation is possible. A high light output cut reduces the detector efficiency and this effect must be taken into account using a simulation as discussed in Sec. IV. For some light-output cuts we have an uncertainty due to the PSD cut on the order of a few percent. For higher light-output cuts the separation of neutrons and γ rays is nearly perfect.

F. Photon flux monitoring

We used three distinct methods for measuring the photon flux. For relative flux measurements, used to subtract background neutrons produced primarily by the photodisintegration of atmospheric nitrogen, we used a three-paddle plastic

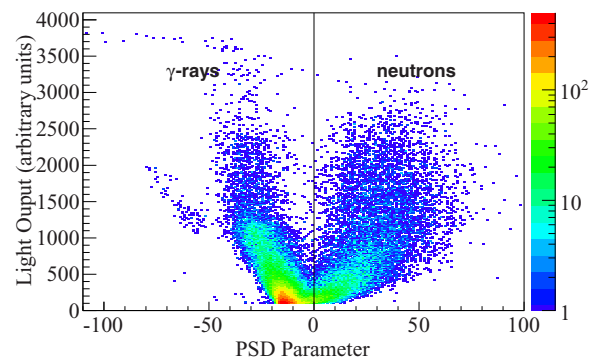


FIG. 3. (Color online) Example PSD spectrum. All γ rays have negative PSD parameter and all events with positive PSD parameter are neutron events. Some neutron events have negative PSD parameter at low light outputs. Light-output cuts are chosen to ensure that the separation of γ rays and neutrons by PSD will introduce uncertainties in the measured neutron yields of only a few percent at most.

scintillating flux monitor placed upstream of the target. This flux monitor was not used for absolute flux determination.

For the data taken with photon energies $20 \text{ MeV} \leq E_\gamma \leq 35 \text{ MeV}$ we employed a five-paddle flux monitor described previously [16]. This flux monitor was placed downstream of the target and an absorption correction was performed to account for photons scattered by the target and by the air. This flux monitor uses a radiator to convert photons into electrons through Compton scattering and pair production. The electrons were detected using a triple coincidence from three scintillator paddles downstream of the radiator. One paddle upstream of the radiator was used as a veto.

We also used the neutron detector cells themselves as a flux monitor. Normally, we used a gate fixed in time to the start signal from the accelerator to hardware prescale Compton scattered γ -ray events to reduce our dead time and increase our sensitivity to neutron events. However, we also took data with this hardware prescale function turned off in order to compare the relative yields of γ -ray events to neutron events. The cross sections for Compton scattering and pair production are well known. After accounting for finite geometry and detector efficiency effects, the γ -ray yields were used to calculate the photon flux multiplied by the target thickness. This quantity was then used to calculate absolute photoneutron cross sections by measuring the neutron yields from the same data acquisition run. The neutron yields for each detector were small in these runs with the hardware prescale turned off. However, if we have already determined the angular dependence of the differential cross section, we can conceptually treat all the detector cells as a single detector and the overall neutron yield is satisfactory for determining the absolute cross section.

III. REACTION CHANNELS

In order to build a model to describe the photodisintegration of ${}^6\text{Li}$ data, we begin with a qualitative analysis. There is certainly structure in the kinetic energy spectrum of the detected neutrons. The neutron kinetic energy spectra in Fig. 4, as computed from time-of-flight spectra, have two prominent features. The high energy feature is due mainly to neutrons emitted from the single-neutron knockout reaction, ${}^6\text{Li} + \gamma \rightarrow n + {}^5\text{Li}$, while the lower energy feature is due mainly to neutrons from the decay of ${}^5\text{He}$ following the single-proton knockout reaction, ${}^6\text{Li} + \gamma \rightarrow p + {}^5\text{He}$. As a result, the high energy feature shows dependence on photon polarization while the low energy feature does not. The low-energy drop off at approximately 2 MeV is due to the detector efficiency dropping to zero because of the low light output cut. The feature below about 1 MeV is due to neutrons taking a longer path to the detector cell due to scattering, and therefore the longer flight time makes them appear to be low energy neutrons. Neutron scattering effects are well described by the detector simulation described in Sec. IV.

We build a model of the photodisintegration of ${}^6\text{Li}$ using these two competing processes. The progeny nuclei ${}^5\text{Li}$ and ${}^5\text{He}$ are particle unstable and immediately decay to the α particle by ejecting a nucleon. The review of Tilley *et al.* [17] lists theoretical values for the excited state energies and decay information for ${}^5\text{Li}$ and ${}^5\text{He}$. We find that the eight reaction

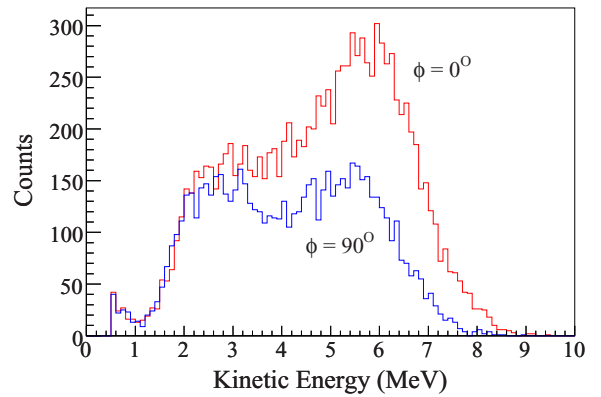


FIG. 4. (Color online) Experimental neutron kinetic energy spectra reported for two neutron detectors at a polar angle $\theta_{\text{lab}} = 90^\circ$. One detector is at an angle-to-polarization of $\phi = 0^\circ$ (red online) while the other is at $\phi = 90^\circ$ (blue online) with a linearly polarized photon beam of energy 13 MeV. Neutron kinetic energy spectra are computed from time-of-flight spectra. The drop off at approximately 2 MeV is due to the detector efficiency dropping to zero. The apparent lower energy neutrons are due to neutron scattering as explained in the text.

channels listed in Table I are the only neutron-producing two-body reaction channels that are likely to be possible over the photon energy range studied here. Indeed we find that these reaction channels are sufficient to describe the data we observe.

We must also consider the possibility of three-body reactions and their contributions at the energies of interest. Proctor and Voelker [18] studied the photodisintegration of ${}^6\text{Li}$ using a bremsstrahlung spectrum with a maximum photon energy of 17.3 MeV. Wade *et al.* [19] studied the quasideuteron reaction at photon energies between 25 and 65 MeV. From these works, we conclude that the cross section for a strongly correlated three-body reaction channel is small enough that we can safely neglect it.

It is not possible with existing data to determine if an uncorrelated, or a weakly correlated, three-body reaction channel contributes to the total cross section. However, we find that an uncorrelated three-body reaction channel, where the three outgoing particles are constrained only by phase space, is neither necessary nor sufficient to explain our data. Since

TABLE I. Reaction channels used to model the photodisintegration of ${}^6\text{Li}$.

Label	Reaction	Threshold (MeV)
(γ, p_0)	${}^6\text{Li} + \gamma \rightarrow p + {}^5\text{He}(\text{g.s.}) \rightarrow n + p + {}^4\text{He}$	4.6
(γ, n_0)	${}^6\text{Li} + \gamma \rightarrow n + {}^5\text{Li}(\text{g.s.})$	5.7
(γ, p_1)	${}^6\text{Li} + \gamma \rightarrow p + {}^5\text{He}(1.27) \rightarrow n + p + {}^4\text{He}$	5.9
(γ, n_1)	${}^6\text{Li} + \gamma \rightarrow n + {}^5\text{Li}(1.49)$	7.0
(γ, p_2)	${}^6\text{Li} + \gamma \rightarrow p + {}^5\text{He}(16.8) \rightarrow n + p + {}^4\text{He}$	21.4
(γ, n_2)	${}^6\text{Li} + \gamma \rightarrow n + {}^5\text{Li}(16.9)$	22.6
(γ, p_3)	${}^6\text{Li} + \gamma \rightarrow p + {}^5\text{He}(19.1) \rightarrow n + p + {}^4\text{He}$	23.7
(γ, n_3)	${}^6\text{Li} + \gamma \rightarrow n + {}^5\text{Li}(19.3)$	25.0

the data are well described by the two-body reaction channels listed in Table I, we neglect uncorrelated and weakly correlated three-body reaction channels. Since there is no correlation, we assume that in the decay of the ${}^5\text{Li}$ and ${}^5\text{He}$ progeny nuclei, the outgoing nucleon is isotropic in the center of mass frame.

Sometimes it is difficult or impossible to distinguish neutrons from two different reaction channels as their kinetic energy spectra are very similar. In such instances we use only the minimum number of reaction channels needed to describe the data and we prefer reaction channels with progeny nuclei with lower excitation energies.

In the above discussion we have built a model to study the photodisintegration of ${}^6\text{Li}$. Inspired by our observations of polarization dependence in the neutron kinetic energy spectra, we built the model based on two types of two-body reaction channels: ${}^6\text{Li} + \gamma \rightarrow n + {}^5\text{Li}$ and ${}^6\text{Li} + \gamma \rightarrow p + {}^5\text{He} \rightarrow n + p + {}^4\text{He}$. We use the excited states tabulated by the review of Tilley *et al.* [17] and assume that the three-body decay is negligible.

The cross sections for individual reaction channels reported in this work are model dependent. The energy levels of the excited states of ${}^5\text{He}$ and ${}^5\text{Li}$ are from calculations that do not report uncertainties. As a result, we are not able to take these uncertainties into account in a systematic and principled way.

IV. SIMULATION

We use a GEANT4 [20] simulation to take into account the effects of finite geometry on our measurements. GEANT4 is a Monte Carlo code that tracks particles as they travel through a defined geometry. To make GEANT4 applicable to our measurements, we add the measured light-output response for our detectors [12].

Given an initial photon energy and a specific reaction channel, the initial kinetic energy spectra of neutrons produced in the photodisintegration of ${}^6\text{Li}$ can be computed from relativistic kinematics. For the (γ, n) reaction channels we emit a neutron and a progeny nucleus directly. For the (γ, p) reaction channels we emit a proton and a progeny nucleus; the progeny nucleus then decays into an α particle and a neutron. As discussed in Sec. III we can neglect three-body reaction channels and therefore make the assumption that the decay of the progeny nucleus is isotropic in its rest frame.

This method allows us to emit neutrons with specific angular distributions. We use the associated Legendre function expansion

$$\frac{d\sigma}{d\Omega}(\theta, \phi) = \frac{\sigma}{4\pi} \left[1 + \sum_{k=1}^{\infty} a_k P_k^0(\cos \theta) + \sum_{k=2}^{\infty} e_k P_k^2(\cos \theta) \cos 2\phi \right], \quad (3)$$

where P_k^q are the associate Legendre functions and the a_k and e_k are their coefficients. The angle θ is the polar angle and ϕ is the angle from the polarization vector. The quantity σ is the total cross section while $d\sigma/d\Omega$ is the differential cross section. By emitting neutrons with only one of a_k and e_k

nonzero, we are able to determine the relative neutron yields for a specific angular distribution.

The final result of the simulation is a computed neutron yield for each detector along with time-of-flight and light-output spectra. The simulation is run for each reaction channel and each associated Legendre function coefficient.

V. DATA ANALYSIS

A. Separation of reaction channels

In our earlier study of the ${}^7\text{Li} + \gamma \rightarrow {}^6\text{Li}(\text{g.s.}) + n$ reaction channel [5] we were able to determine the neutron yields for each detector by making a simple cut on the light-output spectra. However, for the photodisintegration of ${}^6\text{Li}$, we were, in general, not able to separate the reaction channels listed in Table I by placing simple cuts on the data, although it was possible in some cases. Because, at most energies, the competing reaction channels had overlapping neutron kinetic energy spectra, we developed a new algorithm for separating such reaction channels based on fitting simulated time-of-flight spectra for each reaction channel to the measured time-of-flight spectra. A number of example fits will be shown in later sections when we discuss the analysis at individual photon energies. In some cases it was found beneficial to include the light output spectra in the fitting procedure to better constrain the fit. The end result is neutron yields for each reaction channel for each detector cell. We then proceed in a way similar to our ${}^7\text{Li} + \gamma \rightarrow {}^6\text{Li}(\text{g.s.}) + n$ analysis [5] to find the angular distributions.

The dominant source of systematic uncertainty in determining neutron yields for our earlier study of ${}^7\text{Li} + \gamma \rightarrow {}^6\text{Li}(\text{g.s.}) + n$ [5] was uncertainty in the value of our light-output cut, which was a result of uncertainties in the detector cell gains, which, in turn, contributes to an uncertainty in the detection efficiency. In that analysis, these systematic uncertainties dominated the statistical uncertainties. In this analysis, however, in the cases where it was necessary to fit simulated time-of-flight spectra to the measured spectra, the dominant source of uncertainty in the neutron yields is the uncertainty in that fit. This uncertainty can be up to 10 times larger than uncertainties due to any other source. To quantify this uncertainty, we rescale the uncertainties in our neutron yields in order to obtain a reduced χ^2 value of one from the fitting of simulated neutron yields to measured neutron yields used to determine the values of the Legendre coefficients.¹ Since we must rescale the uncertainties in neutron yields, uncertainties in our final quantities will be heavily dominated by systematic uncertainties and therefore we do not report the statistical uncertainties.

We do not claim that this method of finding uncertainties for the separation of the reaction channels is optimal. However, it does appear to provide reasonable estimates of the uncertainties. Figure 5 shows the neutron yields obtained by the fitting

¹In practice we find that it is easier to multiply the computed uncertainties for the associated Legendre polynomial coefficients by the square root of the reduced χ^2 . This is mathematically equivalent to scaling the uncertainties but is less easy to justify conceptually.

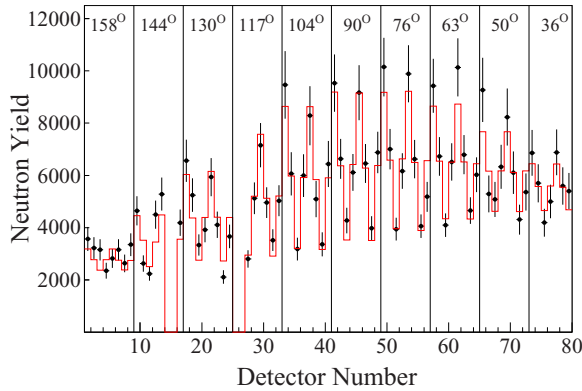


FIG. 5. (Color online) Neutron yields for the reaction channel (γ, n_0) for the detectors of Blowfish used in the analysis at a photon energy of 13 MeV. The data points are the measured yields and the histogram (red online) represents our fit to the data. The uncertainties in the measured yields have been rescaled in order to account for the uncertainty introduced in separating the reaction channels. There are eight detectors at each polar angle and the angle is shown on the plot with vertical lines dividing detectors at different angles. Detectors at specific polar angles are either in the plane of polarization, perpendicular to it, or at 45° to it. Note that detectors numbered 14, 15, 25, and 26 are omitted due to technical issues with those detectors and the detectors numbered 81–88 at angle 22° are also omitted as they did not function reliably due to the large number of gamma-rays scattered into them at this forward angle.

method for the reaction channel (γ, n_0) at a photon energy of 13 MeV. The uncertainties in the neutron yields are rescaled.

Once we have obtained the neutron yields for a reaction channel, as in Fig. 5, we perform a second fit to find the associated Legendre function coefficients. We use the same method as in our previous analysis of ${}^7\text{Li} + \gamma \rightarrow {}^6\text{Li}(\text{g.s.}) + n$. We perform simulations of the reaction channel with the uniform distribution and distributions with only one of a_k and e_k nonzero. We obtain neutron yields for each of the simulated distributions and fit these to the measured neutron yields by adjusting a_k and e_k . Using this method we are able to determine values for a_k and e_k and the relative reaction rates for the different reaction channels.

Once we have obtained the associated Legendre function coefficients and relative rates of each reaction channel, we perform another simulation using these values. The spectra produced by this simulation can be compared with the measured spectra to ensure that our method of separating reaction channels is performing as we expect. Such a comparison is shown in Fig. 6 for a photon energy of 13 MeV. The amplitude of the simulated spectra are scaled to match the measured spectra over the entire array, not on a detector-by-detector basis. In this example the high energy (low time-of-flight) portion is due to the (γ, n_0) reaction channel while the low energy (high time-of-flight) portion is due to the reaction channels (γ, n_1) and (γ, p_1) . It should be noted that the comparison in Fig. 6 is not a fit to this spectrum, examples of which are shown in later sections when we discuss the analysis at individual photon energies. Rather it is the simulation using the angular distribution coefficients obtained from a global

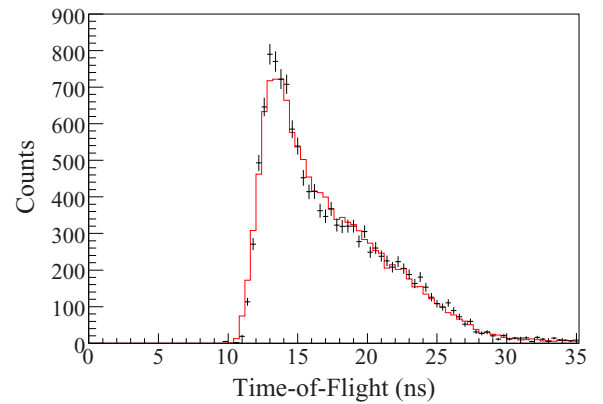


FIG. 6. (Color online) Comparison between a measured time-of-flight spectrum (data points) and a time-of-flight spectrum generated by a simulation using the relative rates and angular distributions of the (γ, n_0) , (γ, n_1) and (γ, p_1) reaction channels (histogram, red online). The uncertainties in the measured data are statistical only. This comparison indicates that our method of separating reaction channels is working as we intend it.

fit to the whole array for all the relevant reaction channels, compared to the data for an individual detector cell.

As we discuss at length in Sec. VI, there is some model dependence inherent in the fitting procedure used to obtain the neutron yields in each cell. As well, as we point out in the analysis discussion for each energy range below, the fits were not always sufficiently constrained to uniquely separate all the reaction channels. For example, where neutron energy spectra from competing reaction channels overlap, they had to be combined to reduce the number of fitting parameters. In other cases, reaction channels whose contributions were known to be very small were set to zero, to help constrain the fit. Nevertheless, even though we may not be able to fully separate all the reaction channels, the end result is an excellent parametrization of the neutron angular distribution. This may be integrated to find the total cross section at each energy which is a primary goal of this measurement. Overall, comparison of our measured spectra with those calculated from our fitted associated Legendre function coefficients (of which Fig. 6 is one example) is reasonable, and we can say that our methods are working as expected.

B. Analysis for E_γ at 8 and 9 MeV

The data at energies 8 and 9 MeV are unique in that they can be described with only a single reaction channel, (γ, n_0) . As such, we can determine the neutron yields with a simple cut on the light-output spectra and do not need to fit time-of-flight spectra. An example of a light-output spectrum is shown in Fig. 7. With reasonable assumptions for the decay widths, the simulation shows that the (γ, p_0) channel contributes insignificantly above the 500 keV_{ee} (equivalent electron energy) light-output cut, and therefore the remaining neutrons in Fig. 7(b) are all from the (γ, n_0) channel and may be integrated to find the (γ, n_0) yield for that cell.

An example time-of-flight spectra showing a comparison between the measured data and a simulation of the (γ, n_0)

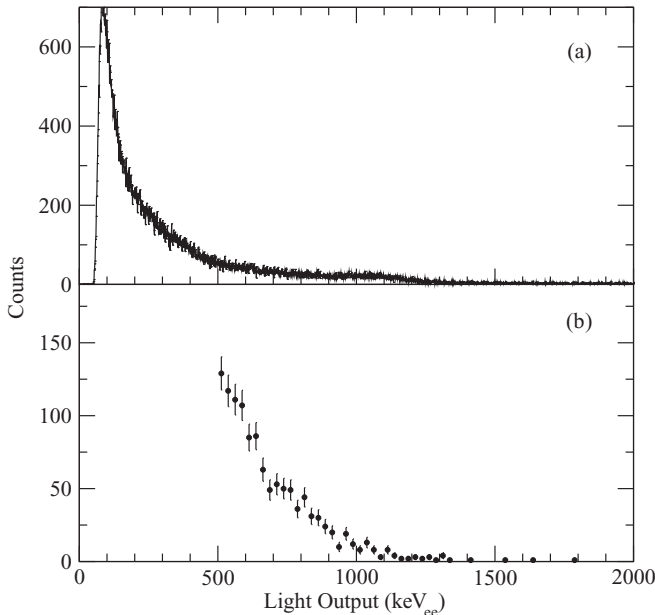


FIG. 7. The light-output spectrum for one cell (cell 42) for one data run at a photon energy of 9 MeV. The light output is in equivalent electron energy units (keV_{ee}). (a) The calibrated light-output spectrum with no cuts applied. (b) The light-output spectrum with a PSD cut applied and a light-output cut of 500 keV_{ee} . With this light-output cut the PSD is essentially perfect so all the counts in this spectrum are neutrons.

reaction channel can be seen in Fig. 8. It is quite possible that the reaction channels (γ, n_1) and (γ, p_1) also contribute neutrons, especially for the photon energy 9 MeV. However, they are impossible to separate from the (γ, n_0) reaction channel so we use the approximation that only the (γ, n_0) reaction channel contributes a substantial number of neutrons.

We compare the measured neutron yields with the simulated neutron yields of our GEANT4 simulation using the reaction

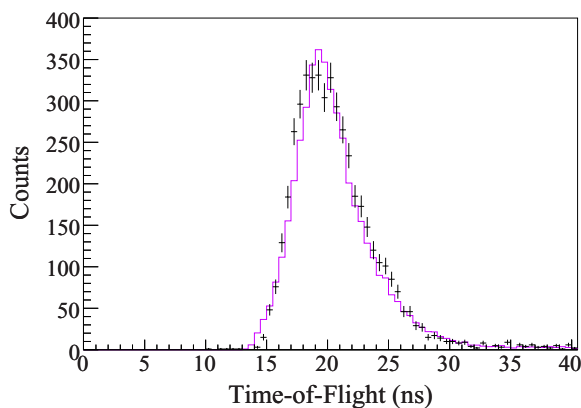


FIG. 8. (Color online) The time-of-flight spectra from the simulation of the (γ, n_0) reaction channel (histogram, purple online) compared with the measured spectrum (data points) taken with a photon energy of 9 MeV. The simulated spectrum was normalized to the measured spectrum. The uncertainties in the measured data are statistical only.

channel (γ, n_0) and each of the associated Legendre functions. By fitting the simulated neutron yields to the measured yields, we can determine values for the associated Legendre function coefficients, a_k and e_k for $k \leq 3$. Once we have found the angular dependence of the cross section, we find the absolute cross section by comparing with the γ -ray yields and scattering cross section.

The largest contribution to the uncertainty in obtaining the angular distribution is systematic uncertainty in the detector efficiency which, especially for these low photon energies, is primarily due to the uncertainty in the cell gains (see Sec. II C). The systematic uncertainties are 3–4 times larger than the statistical uncertainties.

C. Analysis for E_γ from 10 to 15.6 MeV

For the data taken with photon energies 10, 11, 12, 13, 15, and 15.6 MeV we observe three reaction channels, (γ, n_0) , (γ, n_1) , and (γ, p_1) . Again (γ, p_0) likely occurs, but we are not able to detect any neutrons from it due to their low energies. The photon energy 14 MeV was not used due to limited experimental time and 15.6 MeV was used instead of the desired 16 MeV because, at the time, the HIGS storage ring operated more reliably when producing photons at the lower energy.

Our models of the (γ, n_1) and (γ, p_1) reaction channels use the first excited states of ${}^5\text{Li}$ and ${}^5\text{He}$ as the progeny nuclei. These states have large decay widths [17]. Thus, the (γ, n_1) and (γ, p_1) reaction channels have very wide and similar neutron kinetic energy spectra. These spectra become more distinct as the photon energy increases. The spectra are not distinct enough for us to separate them from each other and from the (γ, n_0) reaction channel at photon energies 10, 11, 12, and 13 MeV. At these energies we use (γ, n_0) and an average of (γ, n_1) and (γ, p_1) in our fitting procedure. At photon energies 15 and 15.6 MeV we are able to separate all three reaction channels. Sample plots of measured time-of-flight spectra with time-of-flight spectra from the simulations of the three reaction channels are presented in Figs. 9, 10, and 11.

The fitting procedure is to use the GEANT4 simulated time-of-flight spectra for each reaction channel and fit these to the measured spectra on a detector-by-detector basis. We then compute what proportion of the neutron yield is due to each reaction channel for each detector. It is important to note that we fit only the amplitudes of the simulated spectra to the measured spectra. The energy of the reaction products or the decay widths of the progeny nuclei are not free parameters in the fit.

The resulting neutron yields can be used to determine the associated Legendre function coefficients for each reaction channel. For (γ, n_0) we can determine a_k values with $k \leq 2$ and e_k values with $k \leq 3$. We are not able to obtain a_3 values because noise introduced by the fitting procedure is the dominant source of uncertainty and this coefficient is highly susceptible to such noise. The coefficient e_3 does not appear to be as adversely affected.

Determining angular distributions for (γ, n_1) and (γ, p_1) is not as straightforward as for (γ, n_0) . For (γ, n_0) the fitting procedure is less noisy because it is easier to fit to the high

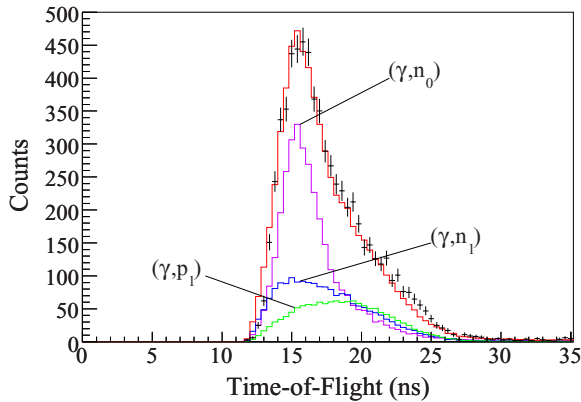


FIG. 9. (Color online) The time-of-flight spectra for the beam energy of 11 MeV. Shown are the simulation of the (γ, n_0) (purple online), (γ, n_1) (blue online), and (γ, p_1) (green online) reaction channels and the measured spectrum (black data points). The histogram through the data points (red online) is the sum of the simulation histograms. The uncertainties in the measured data are statistical only.

energy (low time-of-flight) data than to the broad low energy (high time-of-flight) structure. The fitting procedure introduces large uncertainties into the relative neutron yields extracted for each detector for the reaction channels (γ, n_1) and (γ, p_1) . We are only able to obtain an a_1 value and hesitate to ascribe any physical meaning to this number. Instead, we use this number as a phenomenological input to the simulation in order to reproduce the measured spectra. This parametrization is used when obtaining total cross sections for each reaction channel.

D. Analysis for E_γ from 20 to 35 MeV

The analysis of the data taken with a photon beam of energy $20 \text{ MeV} \leq E_\gamma \leq 35 \text{ MeV}$ proceeds mostly the same as for the

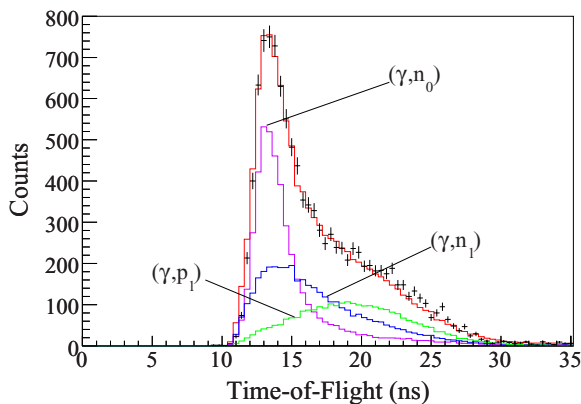


FIG. 10. (Color online) The time-of-flight spectra for the beam energy of 13 MeV. Shown are the simulation of the (γ, n_0) (purple online), (γ, n_1) (blue online), and (γ, p_1) (green online) reaction channels and the measured spectrum (black data points). The histogram through the data points (red online) is the sum of the simulation histograms. The uncertainties in the measured data are statistical only.

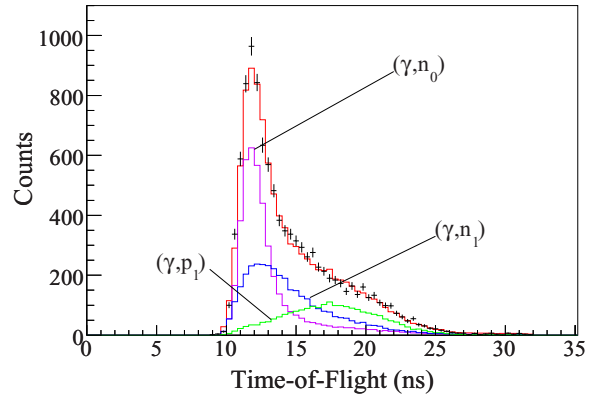


FIG. 11. (Color online) The time-of-flight spectra for the beam energy of 15 MeV. Shown are the simulation of the (γ, n_0) (purple online), (γ, n_1) (blue online), and (γ, p_1) (green online) reaction channels and the measured spectrum (black data points). The histogram through the data points (red online) is the sum of the simulation histograms. The uncertainties in the measured data are statistical only.

lower energies but with some important differences. We have an additional method for monitoring photon flux through the five-paddle flux monitor. We have to perform a subtraction of neutrons produced mostly by the photodisintegration of atmospheric nitrogen. There are also a larger number of reaction channels to consider than at lower energies. The data taken with photon energies of 20 and 25 MeV are adequately described with the (γ, n_0) , (γ, n_1) , and (γ, p_1) reaction channels. The data taken with photon beam energies of $E_\gamma \geq 30 \text{ MeV}$ also require the (γ, n_2) and (γ, p_2) reaction channels and the $E_\gamma = 35 \text{ MeV}$ data also needs (γ, n_3) .

At a photon energy of 20 MeV we cannot separate the (γ, n_0) and (γ, n_1) reaction channels because of their highly overlapping neutron kinetic energy spectra. Instead we must take the average of the two spectra and treat (γ, n_0) and (γ, n_1) as we did for (γ, p_1) and (γ, n_1) at energies from 10 to 13 MeV. At a photon energy of 20 MeV the (γ, p_1) reaction channel is easy to separate and we again see no contribution from (γ, p_0) . The (γ, n_2) and (γ, p_2) reaction channels have thresholds greater than 20 MeV so we do not need to consider them. A sample time-of-flight spectrum can be seen in Fig. 12.

The data with a photon energy of 25 MeV can adequately be described with the (γ, n_1) and (γ, p_1) reaction channels alone. We are unable to obtain reliable fits when the (γ, n_0) reaction channel is included so we make the approximation that its cross section is zero at this photon energy. This does not mean that the (γ, n_0) reaction channel does not occur, but only that it is completely dominated by the (γ, n_1) and (γ, p_1) reaction channels at this energy. Denisov *et al.* [21] measured the cross section of the (γ, p_0) reaction channel. While the magnitude of their absolute cross section does not agree with our observations, their cross section does go to zero near 25 MeV. Since we expect (γ, n_0) and (γ, p_0) to behave similarly (as discussed further in Sec. VII B), this adds further justification for neglecting (γ, n_0) at a photon energy of 25 MeV.

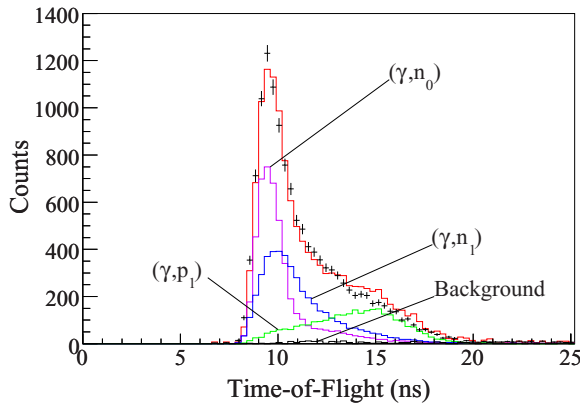


FIG. 12. (Color online) The time-of-flight spectra for the beam energy of 20 MeV. Shown are the simulation of the (γ, n_0) (purple online), (γ, n_1) (blue online), and (γ, p_1) (green online) reaction channels and the measured spectrum (black data points). The histogram through the data points (red online) is the sum of the simulation histograms. The small background contribution from the photodisintegration of atmospheric nitrogen is represented by the black histogram. The uncertainties in the measured data are statistical only.

While the (γ, n_2) and (γ, p_2) reaction channels are allowed at a photon energy of 25 MeV, their cross sections are small enough that they are completely dominated by (γ, n_1) and (γ, p_1) and we do not include them in our fit. A sample time-of-flight spectrum can be seen in Fig. 13.

The data with a photon energy of 30 MeV can be described by the four reaction channels (γ, n_1) , (γ, p_1) , (γ, n_2) , and (γ, p_2) as shown in Fig. 14. Notice that the peak due to (γ, n_2) is very clear and this reaction channel appears to describe the measured spectra well. There is also a contribution to the right of the (γ, n_1) peak that is well described by the (γ, p_2) reaction

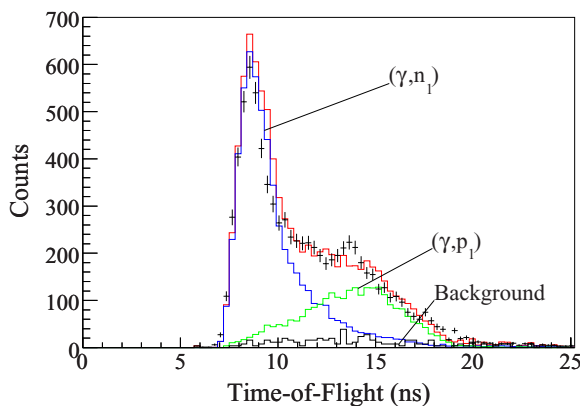


FIG. 13. (Color online) The time-of-flight spectra for the beam energy of 25 MeV. Shown are the simulation of the (γ, n_1) (blue online) and (γ, p_1) (green online) reaction channels and the measured spectrum (black data points). The histogram through the data points (red online) is the sum of the simulation histograms. The small contribution from the photodisintegration of atmospheric nitrogen is represented by the black histogram. The uncertainties in the measured data are statistical only.

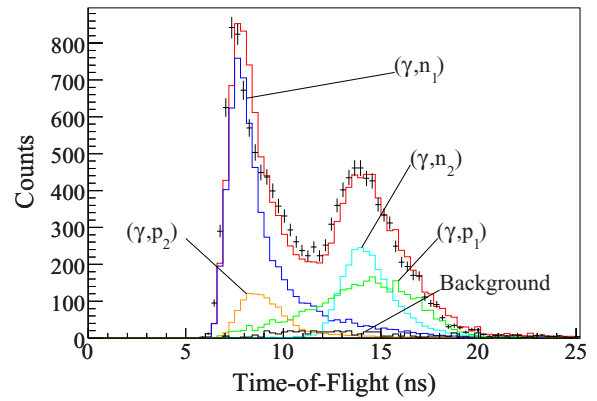


FIG. 14. (Color online) The time-of-flight spectra for the beam energy of 30 MeV. Shown are the simulation of the (γ, n_1) (blue online), (γ, p_1) (green online), (γ, n_2) (cyan online), and (γ, p_2) (orange online) reaction channels and the measured spectrum (black data points). The histogram through the data points (red online) is the sum of the simulation histograms. The small contribution from the photodisintegration of atmospheric nitrogen is represented by the black histogram. The uncertainties in the measured data are statistical only.

channel. For the data at 30 MeV we found it was useful to use fits to both the light-output and time-of-flight spectra to separate the reaction channels. The (γ, n_1) reaction channel is separated mainly using the light-output spectra while the (γ, p_1) , (γ, n_2) , and (γ, p_2) reaction channels are separated using the time-of-flight spectra.

We require five reaction channels to describe the data with a photon energy of 35 MeV: (γ, n_1) , (γ, p_1) , (γ, n_2) , (γ, p_2) , and (γ, n_3) . Because we are including (γ, n_3) , it is likely that we should also consider (γ, p_3) . Since the neutron kinetic energy spectra for (γ, p_2) and (γ, p_3) are so similar, we use the average

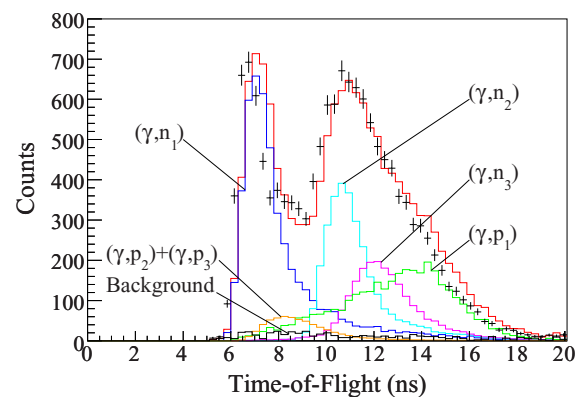


FIG. 15. (Color online) The time-of-flight spectra for the beam energy of 35 MeV. Shown are the simulation of the (γ, n_1) (blue online), (γ, p_1) (green online), (γ, n_2) (cyan online), $(\gamma, p_2) + (\gamma, p_3)$ (orange online), and (γ, n_3) (purple online) reaction channels and the measured spectrum (black data points). The histogram through the data points (red online) is the sum of the simulation histograms. The small contribution from the photodisintegration of atmospheric nitrogen is represented by the black histogram. The uncertainties in the measured data are statistical only.

TABLE II. Associated Legendre function coefficients for the reaction channel (γ, n_0) .

Photon energy (MeV)	a_1	a_2	a_3	e_2	e_3
8	0.070 ± 0.017	-0.199 ± 0.026	0.082 ± 0.036	0.127 ± 0.006	-0.004 ± 0.003
9	0.067 ± 0.011	-0.171 ± 0.018	0.036 ± 0.024	0.095 ± 0.004	-0.004 ± 0.002
10	0.195 ± 0.030	-0.445 ± 0.043	n/a	0.144 ± 0.013	0.002 ± 0.006
11	0.223 ± 0.028	-0.389 ± 0.040	n/a	0.237 ± 0.011	0.002 ± 0.005
12	0.399 ± 0.035	-0.348 ± 0.049	n/a	0.213 ± 0.013	-0.009 ± 0.006
13	0.270 ± 0.033	-0.311 ± 0.046	n/a	0.226 ± 0.011	0.002 ± 0.006
15	0.293 ± 0.036	-0.310 ± 0.051	n/a	0.194 ± 0.012	0.002 ± 0.007
15.6	0.264 ± 0.032	-0.206 ± 0.046	n/a	0.191 ± 0.011	0.012 ± 0.006

spectra for these two reaction channels when determining neutron yields. As can be seen from the plot in Fig. 15 it is becoming increasingly difficult to fit the reaction channels to the measured spectra. The fitting procedure applied at 35 MeV does not perform as reliably as at lower photon energies. We also use both the light-output and time-of-flight spectra to perform the fits at 35 MeV.

Once we obtain the relative cross section for each reaction channel, we obtain the total cross section by comparison with the γ -ray yields and through explicit flux monitoring using the five-paddle flux monitor.

VI. RESULTS

At each photon energy we are able to obtain associated Legendre function coefficients for the reaction channel which produces the highest energy (lowest time-of-flight) neutrons by applying a simple cut on the light output. For photon energies

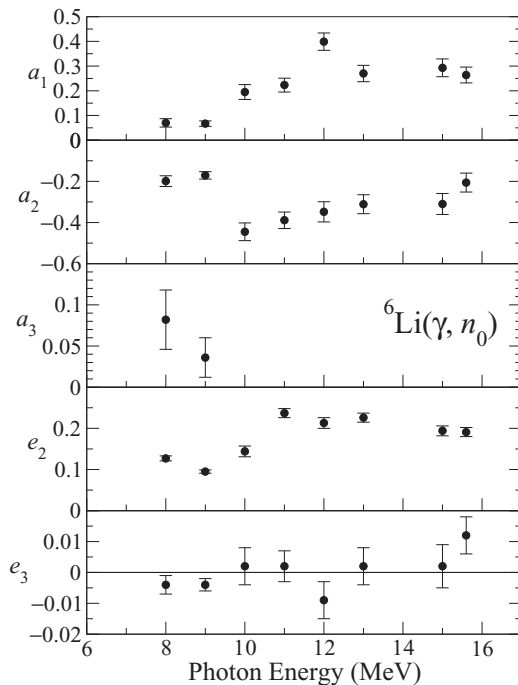


FIG. 16. Associated Legendre function coefficients for the reaction channel (γ, n_0) .

$8 \text{ MeV} \leq E_\gamma \leq 15.6 \text{ MeV}$ this reaction channel is (γ, n_0) and the corresponding coefficients are listed in Table II and plotted in Fig. 16. For energies $25 \text{ MeV} \leq E_\gamma \leq 35 \text{ MeV}$ this reaction channel is (γ, n_1) and the corresponding coefficients are listed in Table III. For the photon energy 20 MeV, we do not report any coefficients as it is not possible to separate the (γ, n_0) and (γ, n_1) reaction channels. At other energies the simulation was able to well fit the measured light output spectra above the applied light output cut. We place no restrictions on the possible values of the Legendre function coefficients in the fit other than requiring that the results are statistically significant.

The reaction channels which have neutrons with kinetic energies lower than that from the (γ, n_0) and (γ, n_1) reaction channels are more difficult to separate from our spectra. Therefore, we are unable to reliably report any angular distribution coefficients for these reaction channels. However we obtain phenomenological values that we do not report here but they are available elsewhere [10]. We use these phenomenological values to reproduce the measured spectra with our simulation, as shown for example in Fig. 6.

In Sec. III we discussed that, because of an unknown level of uncertainty in the properties of the ${}^5\text{Li}$ and ${}^5\text{He}$ progeny nuclei, our final cross sections will be dependent on the model used. As well, at times we had to neglect reaction channels that were dominated by other reaction channels and this also constitutes a model dependence. We list here some of our observations on the model dependence in the absolute cross sections reported in Table IV and plotted in Fig. 17.

- (i) The (γ, n_0) cross section drops between 9 and 10 MeV. This likely indicates that the (γ, n_1) and (γ, p_1) reaction channels contribute at 9 MeV and possibly 8 MeV. We

TABLE III. Associated Legendre function coefficients for the reaction channel (γ, n_1) . Coefficients e_k are not available because we used circularly polarized photons at these energies.

Photon energy (MeV)	a_1	a_2
25	0.111 ± 0.010	-0.460 ± 0.014
30	0.105 ± 0.018	-0.439 ± 0.027
35	0.24 ± 0.10	-0.22 ± 0.15

TABLE IV. Cross sections for the various observable reaction channels for the photodisintegration of ${}^6\text{Li}$. Split columns represent reaction channels that could not be separated and the cross section is a sum for both channels. Estimated contributions from the (γ, n_0) reaction channel have been taken into account. The ‘Observable’ column represents the sum of the (γ, n_0) , (γ, n_1) , (γ, n_2) , (γ, n_3) , (γ, p_1) , (γ, p_2) and (γ, p_3) reaction channels [excluding (γ, p_0)].

Photon energy (MeV)	Observable (mb)	(γ, n_0) (mb)	(γ, n_1) (mb)	(γ, p_1) (mb)
8	0.499 ± 0.098	0.499 ± 0.098	n/a	n/a
9	0.646 ± 0.071	0.646 ± 0.071	n/a	n/a
10	0.955 ± 0.097	0.517 ± 0.028		0.438 ± 0.089
11	1.254 ± 0.070	0.470 ± 0.022		0.786 ± 0.058
12	1.416 ± 0.062	0.535 ± 0.023		0.881 ± 0.047
13	1.448 ± 0.048	0.545 ± 0.017		0.903 ± 0.039
15	1.558 ± 0.067	0.505 ± 0.018	0.438 ± 0.018	0.612 ± 0.055
15.6	1.534 ± 0.073	0.538 ± 0.023	0.422 ± 0.023	0.573 ± 0.052
20	1.555 ± 0.042		0.788 ± 0.023	0.787 ± 0.029
25	1.602 ± 0.040	n/a	0.693 ± 0.018	0.909 ± 0.025
30	1.631 ± 0.046	n/a	0.551 ± 0.019	0.811 ± 0.041
35	1.884 ± 0.050	n/a	0.341 ± 0.023	1.046 ± 0.036
Photon energy (MeV)	(γ, n_2) (mb)	(γ, p_2) (mb)	(γ, p_3) (mb)	(γ, n_3) (mb)
30	0.153 ± 0.008	0.114 ± 0.005	n/a	n/a
35	0.149 ± 0.006		0.110 ± 0.006	0.227 ± 0.008

had to neglect these reaction channels as it was not possible to separate them.

- (ii) Our cross section extraction depends on the correctness of the first excited states of ${}^5\text{Li}$ and ${}^5\text{He}$ that are taken from theoretical calculations as reported in [17]. If these are incorrect the extracted cross sections for (γ, n_1) and (γ, p_1) may be affected. This

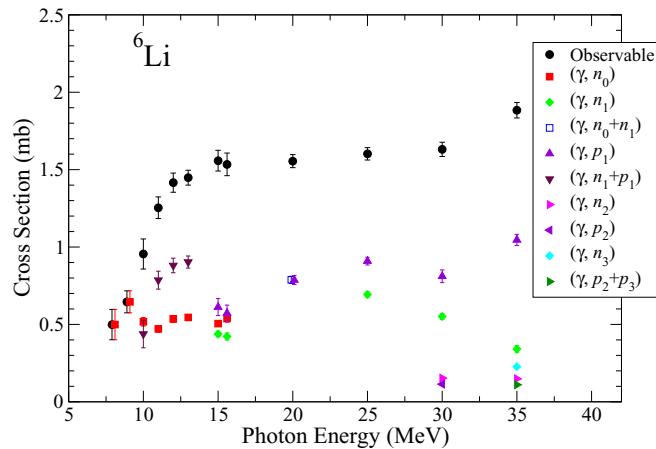


FIG. 17. (Color online) Cross sections for the reaction channels that could be extracted from our data at each energy. It was not possible to separate all reaction channels at all energies, therefore some reaction channels are combined at some energies. The points labeled ‘Observable’ represents the sum of the extracted reaction channel [i.e., all reaction channels that produce neutrons, excluding the (γ, p_0) channel]. Where data points are overlapping they have been displaced in energy for clarity (color online). Note that there is some model dependence in the extraction of reaction channels (see text for discussion).

would especially have an effect on the (γ, p_1) reaction channel because much of the neutron’s kinetic energy comes from the exothermic decay of ${}^5\text{He}$.

- (iii) At a photon energy of 25 MeV we had to neglect the (γ, n_0) , (γ, n_2) , (γ, p_2) , and (γ, p_3) reaction channels as we were not able to separate their spectra from the (γ, n_1) and (γ, p_1) reaction channels. This has likely caused an overestimation of the (γ, n_1) and (γ, p_1) reaction channels at this energy. This is evident in Fig. 17 by the higher values of the (γ, n_1) and (γ, p_1) cross sections at 25 MeV than the surrounding energies. Note that we are able to see what might be a small contribution from (γ, n_2) in the time-of-flight spectrum of Fig. 13 but that it is too small to reliably separate.
- (iv) One must be careful when interpreting the results at a photon energy of 35 MeV. We fit five simulated spectra in order to reproduce the measured spectra. This allows for uncertainty in the excited states of ${}^5\text{He}$ and ${}^5\text{Li}$ to greatly influence our results.
- (v) We must also note that there are a great number of excited states of ${}^5\text{He}$ and ${}^5\text{Li}$ that we are not taking into account and that could have an effect on our results at photon energies of 30 and 35 MeV. The review of Tilley *et al.* [17] lists nine excited states of ${}^5\text{He}$ between 19 and 25 MeV and eight excited states of ${}^5\text{Li}$ between 19 and 26 MeV. Some of these reaction channels could be producing neutrons which have too little energy to detect with our detectors.
- (vi) In order to separate the reaction channels we have ignored the three-body reaction channels. If a three-body reaction channel was found to produce non-negligible numbers of neutrons, it could influence our results at all photon energies.

Rather than construct arbitrary and artificial estimates of the uncertainties due to these caveats, we present our results as is with the above discussion on the model dependence of our results.

Nevertheless, the parametrization of the angular distributions using the phenomenological parameters, as described in Sec. V, do describe the data well. Therefore the total observable cross section, shown by the black filled circles in Fig. 17, is weakly model dependent. This is the total cross section for all reaction channels that produce neutrons, excluding the (γ, p_0) channel.

VII. DISCUSSION

A. Legendre coefficients for ${}^6\text{Li}(\gamma, n_0)$

In the Legendre coefficient fit, that we presented in Table II and Fig. 16, we have made no assumptions about which transition matrix elements (TME) contribute to the cross section. Under the assumption that the cross section consist mainly of p -wave $E1$ absorption along with contributions from s -wave $M1$ and d -wave $E2$, and the TME amplitudes are the same for different p -wave and different d -wave amplitudes, it can be shown [22–24] that $a_1 = -a_3$, $a_3 = -6e_3$, and $a_4 = -12e_3$. If the p -wave $E1$ absorption is dominant over the d -wave $E2$ component we would expect that $a_2 \approx -2e_2$. This is indeed what we observe. The fact that d -wave $E2$ absorption is small is also consistent with our observations that a_2 is negative, and that, within uncertainties, e_3 is close to zero at all energies. At the two energies where we were able to extract an a_3 coefficient the results are consistent with $a_3 = -6e_3$ but are inconsistent with $a_1 = -a_3$. This could indicate a breakdown in the assumptions which led to this result such as the absence of any splittings in the p -wave and/or d -wave TMEs.

B. Photoneutron cross section

We desire to compare our results with previous measurements and theoretical calculations. Since a similar decomposition of the ${}^6\text{Li}$ photodisintegration reaction into individual reaction channels has not been performed, we must construct the total photoneutron cross section in order to perform a comparison with other measurements.

The data labeled ‘Observable’ in Table IV and Fig. 17 contain all photoneutron reaction channels except (γ, p_0) . This would include three-body reaction channels that produce neutrons since they would have been included as a contribution to the fitted reaction channels. If there are significant contributions from three-body reaction channels that produce multiple neutrons these will have been double counted in our ‘Observable’ cross section. A search in our data for multiple neutron events in Blowfish was negative indicating that multiple neutron producing cross sections must be small.

While there are several studies of the ${}^6\text{Li} + \gamma \rightarrow p + {}^5\text{He}$ reactions [21,25–31] we found that we could not use any of them to obtain a cross section for (γ, p_0) . The works of Denisov *et al.* [21] and Junghans *et al.* [29] are the most relevant. However, it is not clear which reaction channels Junghans

et al. are observing. Denisov *et al.* suggest that at 10 MeV the (γ, p_0) cross section is greater than our measured cross sections for the (γ, n_0) , (γ, n_1) and (γ, p_1) reaction channels; therefore their findings are incompatible with the present results. One interesting point that can be taken from the work of Denisov *et al.* is that their measurement of the cross section for (γ, p_0) goes to zero near 25 MeV.

Since we are not able to use previous measurements to estimate the cross section of the (γ, p_0) reaction channel, we will estimate it using the assumption that it is similar to our measurement of (γ, n_0) . The ratio of the cross sections for (γ, p_0) to (γ, n_0) might be expected to be similar to the ratio of (γ, p_1) to (γ, n_1) since p and n decays go to states with the same spin and parity ($3/2^-$ for n_0 and p_0 and $1/2^-$ for n_1 and p_1) and the energy difference between the p and n final states are also similar. Since we have observed that the (γ, p_1) and (γ, n_1) cross sections are similar we make the estimate that the (γ, p_0) and (γ, n_0) cross sections are about the same, and go to zero at about 25 MeV as suggested by the Denisov *et al.* result [21].

We compare our estimated total photoneutron cross section with that of the Livermore group [32] in Fig. 18. The cross-hatched area in that figure illustrates the systematic uncertainty in our estimate due to the $\sigma[(\gamma, p_0)] \simeq \sigma[(\gamma, n_0)]$ assumption. For the purposes of the illustration we assign that systematic uncertainty to be 50% of the measured (γ, n_0) cross section.

Our data agrees with the Livermore group very well at photon energies from 8 to 11 MeV. Since our data points fall directly on their data, it may be the case that our estimate of the cross section for (γ, p_0) is satisfactory and $\sigma[(\gamma, p_0)] \simeq \sigma[(\gamma, n_0)]$. At 12 and 13 MeV we start to see some

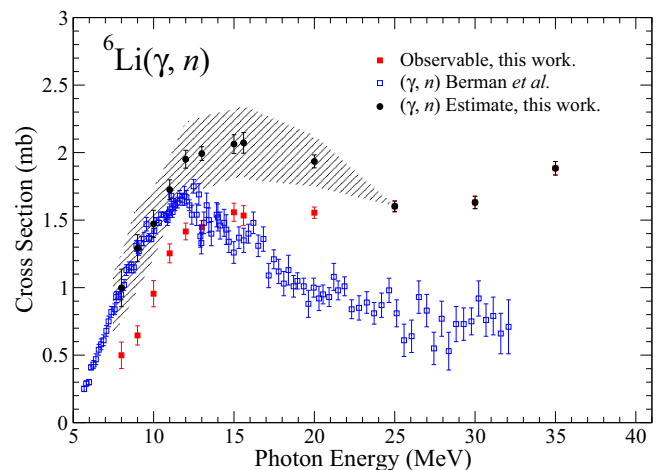


FIG. 18. (Color online) The total photoneutron cross section for ${}^6\text{Li}$ estimated from our data (closed circles) compared with that of the Livermore group [32] (open squares, blue online). The closed squares is our observable photoneutron cross section (red online). The total photoneutron cross section is estimated assuming that the unmeasured (γ, p_0) reaction channel is similar to the (γ, n_0) cross section. The cross-hatched area illustrates the systematic uncertainty inherent in this assumption; it shows an uncertainty equal to 50% of the (γ, n_0) cross section.

divergence of the two data sets, even though they remain within each other's uncertainties. Either our estimate of the (γ, p_0) reaction channel is not as good at these energies, or we are seeing disagreement in the measurements. At photon energies of 15 MeV and above, there is clear disagreement in the two measurements and our cross section is significantly greater than that of the Livermore group. The detector efficiency of the Livermore neutron detector depends on a knowledge of the neutron energy [33]. Only an average neutron energy can be estimated from their neutron detector data. Where only a few competing reaction channels are present, as is the case for ${}^6\text{Li}$ at these energies, the use of an average value may not be appropriate for determining the neutron detector efficiency for detecting ${}^6\text{Li}$ photodisintegration neutrons. However a factor of two error in that efficiency by the Livermore group would appear to be unlikely. Nevertheless, other recent measurements on light nuclei have shown similar levels of disagreement with the Livermore photoneutron cross sections [34,35]. The discrepancy between our results and those of the Livermore group remains unresolved at this time.

C. Total cross section

We now wish to compute a total cross section in order to compare with the theoretical calculation using the Lorentz integral transform technique [4]. We must take into account all reaction channels that do not produce neutrons. Three such reaction channels are the two-body reaction channel ${}^6\text{Li} + \gamma \rightarrow {}^3\text{He} + {}^3\text{H}$ and the three-body reaction channels ${}^6\text{Li} + \gamma \rightarrow p + d + {}^3\text{H}$ and ${}^6\text{Li} + \gamma \rightarrow 3d$. The latter is not an electric dipole reaction [36] and is therefore unlikely to be significant.

The reaction channel ${}^6\text{Li} + \gamma \rightarrow p + d + {}^3\text{H}$ has been studied by a number of authors [37–41]. The measurement of Marakami [37,38] is not consistent with our measurements as this author finds a maximum cross section of this reaction channel of 6 mb at a photon energy of 25 MeV. This cross section is far too large and is possibly affected by uncertainties in the normalization to the ${}^{12}\text{C} + \gamma \rightarrow 3\text{ }^4\text{He}$ reaction channel used to obtain the flux. It is not clear that the results of Volkov *et al.* [39] are model independent and the final cross sections may assume an α -particle photodisintegration process model. Kotikov and Makhnovskiĭ [40] present another interesting work but their cross sections are based on only 18 measured photodisintegration events. Between these poor statistics and questions about systematic uncertainties, we cannot use these cross sections to aid us. The results of Rychbosch *et al.* [41] give a cross section of about 300 μb at a photon energy of 48 MeV, which is too high of an energy for our use but indicates that the cross section is fairly small at higher energies.

It is interesting to note that both the work of Kotikov and Makhnovskiĭ and the work of Marakami measure similar energy dependencies of the ${}^6\text{Li} + \gamma \rightarrow p + d + {}^3\text{H}$ cross section. The cross section rises quickly from its threshold at 21.3 MeV and peaks between photon energies of 24 and 25 MeV. Unfortunately, the absolute values of the cross sections disagree with each other by more than a factor of

two and neither of them are consistent with our observations based on other reaction channels. If this reaction channel does have an effect on our data, it will be on the data with a photon energy of 25 MeV. Given that we have not yet included any three body reaction channels and there is not a satisfactory measurement of the cross section of ${}^6\text{Li} + \gamma \rightarrow p + d + {}^3\text{H}$, we are forced to neglect it.

We must now find a cross section for the two-body reaction channel that does not produce neutrons, ${}^6\text{Li} + \gamma \rightarrow {}^3\text{He} + {}^3\text{H}$. Komar and Makhnovskiĭ [42] found a cross section which peaks at 8 mb at a photon energy of 21 MeV. Murakami [37,38] found a cross section which peaks at 5 mb at a photon energy of 21 MeV. Because these authors have measured cross sections that are so large, we will not include them in our analysis because their absolute normalizations likely suffer difficulties. However, we find the fact that they both observe peaks at 21 MeV useful.

Titterton and Brinkley [43] do not observe the reaction at a photon energy of 17.6 MeV, which indicates that the cross section is near zero at this energy which is close to the threshold of 15.8 MeV. Manuzio *et al.* [44] found the cross section for this reaction channel from 25.2 to 30 MeV. Sherman *et al.* [36,45] found the cross section from a photon energy of 19 to 35 MeV. Shin, Skopik and Murphy [46] found the differential cross section at 90° for photon energies from 23.1 MeV to 68.2 MeV while Junghans *et al.* [29] supply the same quantity with the angular distributions required to convert it into an absolute cross section. We use the Legendre function coefficient value $a_2 = -1$ suggested by Junghans *et al.* [29] to convert differential cross sections into absolute cross sections through $\sigma = \frac{8\pi}{3} \frac{d\sigma}{d\Omega}(\theta = 90^\circ)$. These results are plotted in Fig. 19. Since these values are not in agreement, we construct composite values using the average as our recommended value, with the difference between the highest and lowest as the uncertainty. Our composite values are also shown in Fig. 19.

We compare the total cross section, which we have constructed from our measurements and the measurements of

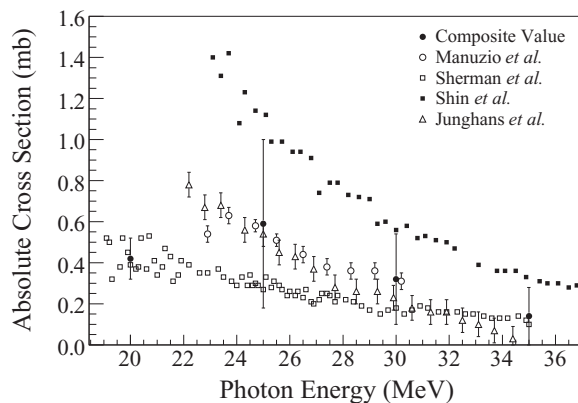


FIG. 19. Absolute cross section for the reaction channel ${}^6\text{Li} + \gamma \rightarrow {}^3\text{He} + {}^3\text{H}$ from Manuzio *et al.* (open circles) [44], Sherman *et al.* (open squares) [36,45], Shin, Skopik, and Murphy (closed squares) [46], and Junghans *et al.* (open triangles) [29] with our composite values (closed circles).

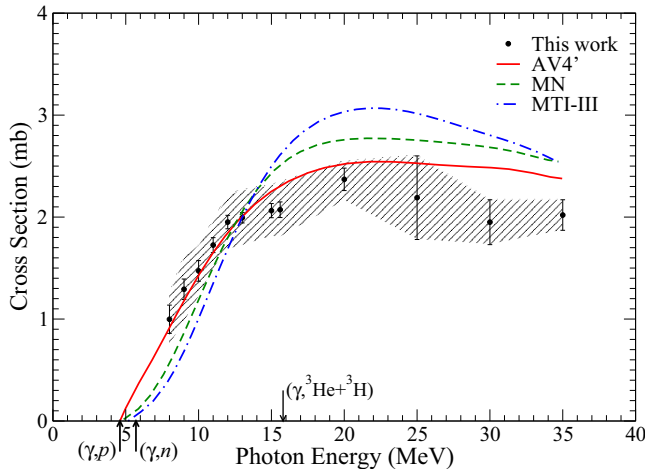


FIG. 20. (Color online) Our constructed total ${}^6\text{Li}$ photodisintegration cross section for all reaction channels (closed circles). Error bars are calculated using the assumed values for the (γ, p_0) cross section and the $(\gamma, {}^3\text{He} + {}^3\text{H})$ as discussed in the text. The cross-hatched area illustrates the systematic uncertainty which is dominated below 20 MeV by the assumption that the (γ, p_0) cross section is similar to the (γ, n_0) cross section, and above 20 MeV by the uncertainty in the average measured $(\gamma, {}^3\text{He} + {}^3\text{H})$ cross sections. These data are compared with the prediction of the Lorentz integral transform calculation [4] using the AV4' model (line, red online), the MN model (dashed line, green online), and the MTI-III model (dot-dashed line, blue online). Reaction threshold energies are shown by the arrows.

others, with the predictions of the Lorentz integral transform calculation for three nucleon-nucleon potential models in Fig. 20. We see that there is reasonable agreement with the AV4' potential model at all photon energies except 30 and 35 MeV. There are several possible reasons for this. At these high energies there are many reaction channels possible and therefore the fitting to our measured neutron energy spectrum is more challenging. It is possible that the fit could be improperly distributing neutrons between reaction channels and therefore our simulated neutron detection efficiency could be compromised. There could also be a contribution from ${}^6\text{Li} + \gamma \rightarrow p + d + {}^3\text{H}$ that we are unable to take into account using previous measurements. Therefore a definitive interpretation of the total photon absorption cross section is compromised by the large uncertainties, which are dominated at photon energies below 25 MeV by our need to estimate the cross section for (γ, p_0) , and at higher photon energies by the uncertainty in the cross section of ${}^6\text{Li} + \gamma \rightarrow {}^3\text{He} + {}^3\text{H}$ and the need to neglect non-neutron-producing three body reaction channels.

VIII. CONCLUSION

We have measured the photoneutron cross sections of ${}^6\text{Li}$ for reaction channels that produce neutrons using the large solid angle neutron detector Blowfish and the High Intensity Gamma Source photon beam. Using a GEANT4 simulation we can predict the neutron energy distribution expected in each detector cell for each reaction channel. A fit to the measured neutron energy distribution, found using time of flight, yields the contribution for each reaction channel. These yields for each cell are then fitted to extract a parametrization of the angular distribution for each reaction channel. This distribution is integrated to extract cross sections for each reaction channel. It is only possible to extract cross sections for reaction channels that have sufficient numbers of neutrons above our detection threshold to form a statistically significant contribution to each cell. Thus we were not able to extract the (γ, p_0) cross section. Uncertainties in the reaction cross sections are dominated, not by statistical uncertainties, but by the uncertainties in the fits and by the systematic uncertainty in the photon flux.

Comparison with a previously measured photoneutron cross section relies on an estimate of the unmeasured (γ, p_0) cross section. Our results are consistent with earlier measurements below 12 MeV but have a larger cross section at higher energies.

A comparison with the total photon absorption cross section predicted by Bacca *et al.* [4] for various nucleon-nucleon interaction models is further hampered by our lack of knowledge of the non-neutron producing reaction channels that we do not measure. The most important of these is the reaction channel ${}^6\text{Li} + \gamma \rightarrow {}^3\text{He} + {}^3\text{H}$. Unfortunately there are serious disagreements between measurements of this cross section in the literature. Therefore a comparison to the total cross section calculation is inconclusive.

Nevertheless, we have shown that precision cross sections can be measured for specific reaction channels over certain energy ranges. We hope that the quality of these measurements will provide an incentive for theoretical calculations of the cross sections for specific reaction channels.

ACKNOWLEDGMENTS

We would like to acknowledge the financial support of the Natural Sciences and Engineering Research Council of Canada (NSERC). This research has been enabled by the use of computing resources provided by WestGrid and Compute/Calcul Canada. We would like to thank Johannes Vogt and the staff of the Canadian Light Source for their help in constructing the lithium target. We would also like to thank the staff of the High Intensity Gamma-Ray Source for their collaboration and the excellent operation of the accelerator. This work comprises part of the thesis of Wurtz [10].

- [1] V. D. Efros, W. Leidemann, and G. Orlandini, *Phys. Lett. B* **338**, 130 (1994).
 [2] V. D. Efros, W. Leidemann, G. Orlandini, and N. Barnea, *J. Phys. G* **34**, R459 (2007).

- [3] S. Quaglioni, W. Leidemann, G. Orlandini, N. Barnea, and V. D. Efros, *Phys. Rev. C* **69**, 044002 (2004).
 [4] S. Bacca, N. Barnea, W. Leidemann, and G. Orlandini, *Phys. Rev. C* **69**, 057001 (2004).

- [5] W. A. Wurtz, R. E. Pywell, B. E. Norum, S. Kucuker, B. D. Sawatzky, H. R. Weller, M. W. Ahmed, and S. Stave, *Phys. Rev. C* **84**, 044601 (2011).
- [6] V. N. Litvinenko, B. Burnham, M. Emamian, N. Hower, J. M. J. Madey, P. Morcombe, P. G. O'Shea, S. H. Park, R. Sachtshale, K. D. Straub, G. Swift, P. Wang, Y. Wu, R. S. Canon, C. R. Howell, N. R. Roberson, E. C. Schreiber, M. Spraker, W. Tornow, H. R. Weller, I. V. Pinayev, N. G. Gavrillov, M. G. Fedotov, G. N. Kulipanov, G. Y. Kurkin, S. F. Mikhailov, V. M. Popik, A. N. Skrinsky, N. A. Vinokurov, B. E. Norum, A. Lumpkin, and B. Yang, *Phys. Rev. Lett.* **78**, 4569 (1997).
- [7] Y. Wu, V. N. Litvinenko, S. F. Mikhailov, O. A. Shevchenko, N. A. Vinokurov, N. G. Gavrillov, T. V. Shaftan, and D. A. Kairan, *Nucl. Instrum. Methods Phys. Res. A* **475**, 253 (2001).
- [8] V. N. Litvinenko, S. F. Mikhailov, O. A. Shevchenko, N. A. Vinokurov, N. G. Gavrillov, G. N. Kulipanov, T. V. Shaftan, P. D. Vobly, and Y. Wu, *Nucl. Instrum. Methods Phys. Res. A* **475**, 407 (2001).
- [9] J. C. Bergstrom, R. Igarashi, and J. M. Vogt, *Phys. Rev. C* **59**, 2588 (1999).
- [10] W. A. Wurtz, Ph.D. thesis, University of Saskatchewan (2010).
- [11] B. D. Sawatzky, Ph.D. dissertation, University of Virginia (2005).
- [12] R. Pywell, B. Sawatzky, J. Ives, N. Kolb, R. Igarashi, and W. Wurtz, *Nucl. Instrum. Methods Phys. Res. A* **565**, 725 (2006).
- [13] B. Bewer, R. Pywell, R. Igarashi, and W. Wurtz, *Nucl. Instrum. Methods Phys. Res. A* **608**, 417 (2009).
- [14] D. Murray, in *Computer Applications in Nuclear, Particle and Plasma Physics, Conference Record, Seventh Conference Real Time '91* (1991), pp. 37–45.
- [15] D. Chabot, R. Igarashi, D. Dodds, and W. Norum, in *Canadian Conference on Electrical and Computer Engineering* (IEEE CCECE, Saskatoon, 2005), pp. 2257–2260.
- [16] R. Pywell, O. Mavrichi, W. Wurtz, and R. Wilson, *Nucl. Instrum. Methods Phys. Res. A* **606**, 517 (2009).
- [17] D. R. Tilley, C. M. Cheves, J. L. Godwin, G. M. Hale, H. M. Hofmann, J. H. Kelley, C. G. Sheu, and H. R. Weller, *Nucl. Phys. A* **708**, 3 (2002).
- [18] D. G. Proctor and W. H. Voelker, *Phys. Rev.* **118**, 217 (1960).
- [19] M. W. Wade, M. K. Brussel, L. J. Koester, and J. H. Smith, *Phys. Rev. Lett.* **53**, 2540 (1984).
- [20] S. Agostinel *et al.*, *Nucl. Instrum. Methods Phys. Res. A* **506**, 250 (2003).
- [21] V. P. Denisov, A. P. Komar, L. A. Kul'chitskiĭ, and E. D. Makhnovskiĭ, *Sov. J. Nucl. Phys.* **5**, 349 (1967).
- [22] H. R. Weller, J. Langenbrunner, R. M. Chasteler, E. L. Tomusiak, J. Asai, R. G. Seyler, and D. R. Lehman, *At. Data Nucl. Data Tables* **50**, 29 (1992).
- [23] H. R. Weller, R. M. Chasteler, B. S. Marks, R. G. Seyler, and D. R. Lehman, *At. Data Nucl. Data Tables* **58**, 219 (1994).
- [24] M. Blackston, Ph.D. thesis, Duke University (2007).
- [25] E. B. Bazhanov and L. A. Kul'chitskiĭ, *Sov. Phys. JETP* **11**, 1215 (1960).
- [26] Y. M. Volkov and L. A. Kul'chitskiĭ, *Sov. Phys. JETP* **15**, 77 (1962).
- [27] C. F. Wong, R. M. Hutcheon, Y. M. Shin, and H. S. Caplan, *Can. J. Phys.* **48**, 1917 (1970).
- [28] J. L. Matthews, D. J. S. Findlay, S. N. Gardiner, and R. O. Owens, *Nucl. Phys. A* **267**, 51 (1976).
- [29] G. Junghans, K. Bangert, U. E. P. Berg, R. Stock, and K. Wienhard, *Z. Phys. A* **291**, 353 (1979).
- [30] P. J. Carlos, P. Bourgeois, J. Fagot, J. L. Fallou, P. Garganne, J. M. Laget, A. Lepretre, A. de Miniac, C. Veyssiere, J. Jury, and D. Ryckbosch, *Phys. Lett. B* **203**, 33 (1988).
- [31] J. F. Dias, D. Ryckbosch, R. V. de Vyver, C. V. den Abeele, G. D. Meyer, L. V. Hoorebeke, J. O. Adler, K. I. Blomqvist, D. Nilsson, H. Ruijter, and B. Schröder, *Nucl. Phys. A* **587**, 434 (1995).
- [32] B. L. Berman, R. L. Bramblett, J. T. Caldwell, R. R. Harvey, and S. C. Fultz, *Phys. Rev. Lett.* **15**, 727 (1965).
- [33] B. Berman and S. Fultz, *Rev. Mod. Phys.* **47**, 713 (1975).
- [34] B. Nilsson, J.-O. Adler, B.-E. Andersson, J. Annand, I. Akkurt, M. Boland, G. Crawford, K. Fissum, K. Hansen, P. Harty, D. Ireland, L. Isaksson, M. Karlsson, M. Lundin, J. McGeorge, G. Miller, H. Ruijter, A. Sandell, B. Schröder, D. Sims, and D. Watts, *Phys. Lett. B* **626**, 65 (2005).
- [35] W. Tornow, J. H. Kelley, R. Raut, G. Rusev, A. P. Tonchev, M. W. Ahmed, A. S. Crowell, and S. C. Stave, *Phys. Rev. C* **85**, 061001(R) (2012).
- [36] N. K. Sherman, J. E. E. Baglin, and R. O. Owens, *Phys. Rev.* **169**, 771 (1968).
- [37] A. Murakami, *Nuovo Cimento* **55**, 604 (1968).
- [38] A. Murakami, *J. Phys. Soc. Jpn.* **28**, 1 (1970).
- [39] Y. M. Volkov, G. A. Kolomenskiĭ, E. F. Lakovichev, E. D. Makhnovskiĭ, A. V. Nadtochiĭ, V. V. Popov, V. P. Fominenko, and V. P. Chizhov, *Sov. J. Nucl. Phys.* **27**, 461 (1978).
- [40] E. A. Kotikov and E. D. Makhnovskiĭ, *Sov. J. Nucl. Phys.* **41**, 183 (1985).
- [41] D. Ryckbosch, L. V. Hoorebeke, R. V. de Vyver, C. V. den Abeele, J. Dias, J.-O. Adler, K. I. Blomqvist, D. Nilsson, B. Schröder, and K. Ziakas, *Nucl. Phys. A* **568**, 52 (1994).
- [42] A. P. Komar and E. D. Makhnovskiĭ, *Sov. Phys. Doklady* **9**, 463 (1964).
- [43] E. W. Titterton and T. A. Brinkley, *Aust. J. Phys.* **7**, 350 (1954).
- [44] G. Manuzio, R. Malvano, G. Ricco, and M. Sanzone, *Nuovo Cimento B* **40**, 300 (1965).
- [45] N. K. Sherman, J. R. Stewart, and R. C. Morrison, *Phys. Rev. Lett.* **17**, 31 (1966).
- [46] Y. M. Shin, D. M. Skopik, and J. J. Murphy, *Phys. Lett. B* **55**, 297 (1975).